ANNUAL REVIEWS

Annual Review of Nuclear and Particle Science

Efimov Physics and Connections to Nuclear Physics

A. Kievsky,[1] M. Gattobigio,[2] L. Girlanda,[3,4] and M. Viviani[1]

[1]Istituto Nazionale di Fisica Nucleare, Sezione di Pisa, 56127 Pisa, Italy; email: alejandro.kievsky@pi.infn.it

[2]Université Côte d'Azur, CNRS, Institut de Physique de Nice, 06560 Valbonne, France

[3]Dipartimento di Matematica e Fisica "E. De Giorgi," Università del Salento, 73100 Lecce, Italy

[4]Istituto Nazionale di Fisica Nucleare, Sezione di Lecce, 73100 Lecce, Italy

Annu. Rev. Nucl. Part. Sci. 2021. 71:465–90

First published as a Review in Advance on July 6, 2021

The *Annual Review of Nuclear and Particle Science* is online at nucl.annualreviews.org

https://doi.org/10.1146/annurev-nucl-102419-032845

Keywords

Efimov physics, universal properties, Gaussian characterization, few-body systems, discrete scale invariance, unitary limit

Abstract

Physical systems characterized by a shallow two-body bound or virtual state are governed at large distances by continuous scale invariance, which is broken into discrete scale invariance when three or more particles come into play. This symmetry induces a universal behavior for different systems that is independent of the details of the underlying interaction and rooted in the smallness of the ratio $\ell/a_B \ll 1$, where the length a_B is associated with the binding energy of the two-body system $E_2 = \hbar^2/ma_B^2$, and ℓ is the natural length given by the interaction range. Efimov physics refers to this universal behavior, which is often hidden by the onset of system-specific nonuniversal effects. In this review, we identify universal properties by providing an explicit link of physical systems to their unitary limit, in which $a_B \to \infty$, and we show that nuclear systems belong to this class of universality.

Contents

1. INTRODUCTION

Studying a particular physical system, we could wonder about the interactions that govern the underlying dynamics. Usually, the particular characteristics of those interactions are revealed by the properties of those systems. The case of residual interactions is especially interesting—as exemplified by the nuclear interaction, a residual interaction of quantum chromodynamics (QCD), or by molecular structures built under residual effects of quantum electrodynamics. We can imagine situations in which the residual interaction places the system in a particular energy region where the characteristics of the interaction become unimportant (we may consider this a fine-tuning). Similar situations could occur when a system is subject to a suitable external field. Following these ideas, and focusing on a nonrelativistic theory, we can design a short-range tunable potential describing a two-particle system with mass m and refer to the unitary window as the region in the space of the potential parameters such that the scattering length a reaches a value close to infinity. When a is large, the two-body system has a shallow (real or virtual) bound state whose binding energy is governed by the scattering length: $E_2 \approx \hbar^2/ma^2$. Its shallow character is defined with respect to the typical energy of the system, $\hbar^2/m\ell^2$, where the typical length of the system ℓ could be, for example, the potential range. The limit $\ell/a \to 0$ can be reached in two ways: the scattering length going to infinity (unitary limit) or the interaction range going to zero (zero-range limit or scaling limit). When $\ell/a \ll 1$, the system is inside the unitary window, a particular region in which universal behavior can be observed allowing for a common description of totally different systems, ranging from nuclear physics to atomic physics or down in scale to hadronic systems.

Weakly bound systems define a class of universality; the particles stay most of the time outside the interaction range, and many of their properties can be explained in terms of the probability of being inside the classically forbidden region. The fine-tuning of the potential parameters, which is necessary to bring a system inside the unitary window, can be realized in laboratories using external fields—for instance, for trapped cold atoms with Feshbach resonances (1)—or it can be naturally produced. There are a few natural systems located inside this window; one is the dimer of two helium atoms. In fact, the $^4He_2$ molecule has an extremely low binding energy, $E_2 \approx 1$ mK, several orders of magnitude smaller than the typical interaction energy (2), $\hbar^2/mr_{vdW}^2 \approx 1.5$ K, given in terms of its van der Waals length, $r_{vdW} = 5.08\, a_0$ (here and below, a_0 denotes the Bohr radius). Nuclear physics is another example; the deuteron binding energy is $E_2 = 2.22456$ MeV, which is much smaller than the typical nuclear energy, $\hbar^2/m\ell^2 \approx 20$ MeV (in this case, the interaction length is given by the inverse of the pion mass m_π, $\ell \sim 1/m_\pi \approx 1.4$ fm).

Nuclear physics is the low-energy realization of QCD; in this regime, QCD is a strongly interacting quantum field theory, and therefore nonperturbative approaches are necessary. Such approaches start to appear in the form of lattice QCD (LQCD) (3–7); however, detailed computations of nuclear properties with these techniques do not yet seem feasible. In recent years it has been realized that the interaction among nucleons can be constructed in an effective field theory (EFT) approach that exploits the symmetries of QCD (8–18). In the limit of zero-mass light quarks, the chiral symmetry appears, and its spontaneous breakdown gives rise to Goldstone bosons, the π mesons. The mass of the pion m_π is nonzero because of the soft explicit breaking term introduced by the masses of the up and down quarks, but it is still much lower than the typical hadronic masses. Another interesting limit in QCD can be reached considering that the mass of the pion is close to a critical value at which the nucleon–nucleon scattering lengths diverge (19, 20). The $^1S_0$ (singlet) a_s and $^3S_1$ (triplet) a_t scattering lengths are functions of the up and down quark masses or, equivalently, of m_π, which is related to the quark masses by the Gell-Mann–Oakes–Renner relation (21). It has been shown that for $m_\pi \approx 200$ MeV, both scattering lengths diverge (22, 23). At the physical point, $m_\pi \approx 138$ MeV, the values of the two scattering lengths are $a_s \approx -23.7$ fm and $a_t \approx 5.4$ fm—still appreciably larger than the typical interaction length $\ell \approx 1.4$ fm.

A model-independent description of the physics inside the unitary window is given by an EFT based on the clear separation of scales between the typical momenta $Q \sim 1/a$ of the system and the underlying high-momentum scale $\sim 1/\ell$ (18, 24–26). This condition is well fulfilled in both systems: atomic helium and nuclear physics. In the latter case, this approach is known as pionless EFT (24, 27–29). Using such an EFT, if the power-counting is correct (24, 27, 30–32), one can systematically improve the prediction of the observables. For instance, at low energies where $E = \hbar^2 k^2/m$, the S-wave phase-shift δ, determined by the effective range expansion (ERE) (33)

$$k \cot \delta = -\frac{1}{a} + \frac{1}{2} r_e k^2, \qquad 1.$$

can be reproduced by such an expansion (24). The leading order (LO) term captures the information encoded in the scattering length a, whereas the finite-range nature of the interaction, represented by the effective range r_e, constitutes the next-to-leading order (NLO) term. Inside the unitary window, there is an energy pole close to the two-particle threshold relating the scattering and bound state properties. The extension of the ERE to the negative energy pole results in

$$\frac{1}{a_B} = \frac{1}{a} + \frac{1}{2}\frac{r_e}{a_B^2}, \qquad 2.$$

where $E_2 = \hbar^2/ma_B^2$ defines the energy length a_B. It could be positive (bound state) or negative (virtual state). Moreover, $|a_B| \gg r_e \sim \ell$ and $a \sim a_B$, so the ratio r_e/a_B represents a small parameter.

In this energy region, the two-body system is dominated by continuous scale invariance (CSI) governed by the control parameter a_B with violations of the order of r_e/a_B.

The most remarkable property of systems at the unitary limit appears at the three-body level through the Efimov effect (34, 35). CSI in the two-body system is dynamically broken at the level of three bodies into discrete scale invariance (DSI). When the strength of the two-body interaction is such that there is a bound state at zero energy, an infinite tower of geometrically distributed energy states appears in the three-body system with the energy threshold $E_3 = 0$ as an accumulating point. The energy ratio of successive levels $E_3^{n+1}/E_3^n = e^{-2\pi/s_0}$ is a universal constant, with s_0 depending on the mass ratio of the constituents; for three equal bosons, $s_0 \simeq 1.00624$, so $e^{-2\pi/s_0} \simeq (1/22.7)^2$. The anomalous breaking of the symmetry gives rise to an emergent scale at the three-body level (which is usually referred to as the three-body parameter κ_*), giving the binding energy $\hbar^2\kappa_*^2/m$ of a reference state belonging to the tower of states at the unitary point.

This effect, predicted by Vitaly Efimov around 50 years ago, was observed 35 years after its prediction by the group of Rudolf Grimm (36). An enormous amount of work, experimental as well as theoretical, has been (and still is) dedicated to the study of this phenomenon. An introduction to this sector of research can be found in References 37–45 and the works cited therein. The physics associated with the Efimov effect is called Efimov physics, and the energy region in which the consequences of this effect can be observed is called the universal window, unitary window, or Efimov window. Observing universal behavior of systems that belong to this window can help us to better understand the universal dynamics, as has been shown recently in the analysis of the three- and four-neutron systems. The evidence of a low-energy tetraneutron, observed in two experiments (46, 47), has been attributed to the universal long-range tail of that system (48, 49). Furthermore, arguments based on the separation of scales have been recently exploited to describe halo nuclei, a sector of physics in which universal properties are expected to be observed (see 50–54 and references therein).

To study universal behavior in few-boson and few-fermion systems, the Schrödinger equation has been solved using two different variational methods. For systems with three and four particles, we have used the hyperspherical harmonics (55, 56) method and its unsymmetrized version (57, 58). For heavier systems, we have implemented a version of the stochastic variational method (59) using correlated Gaussian functions as the basis set.

2. UNIVERSAL CHARACTERIZATION OF TWO-BODY SYSTEMS

The dynamics of two-body systems inside the universal window is highly independent of the details of their mutual interaction. The systems satisfy an approximate CSI, which is exactly verified in the case of a zero-range interaction. Though the zero-range case was used many times as a first approximation to describe systems inside the universal window, we proceed differently and start our description from the ERE (Equation 2) relating the three parameters that determine the low-energy dynamics of the system. It can be cast in the following compact form:

$$r_e a = 2 r_B a_B, \qquad 3.$$

where we have introduced the length $r_B = a - a_B$—which, together with the energy length a_B, completely determines the S-matrix of systems that have one bound state (60, 61). In the case of a zero-range interaction, $a = a_B$ and $r_B = 0$. To study the dynamics of the systems inside the universal window, we make use of a two-parameter short-range potential and consider this potential a minimal low-energy representation of the two-particle interaction fixed by two low-energy data points, a_B (or a) and r_B (or r_e).

2.1. The Characteristic Potential

To characterize the universal window, we make use of a Gaussian potential:

$$V(r) = V_0 e^{-r^2/r_0^2}, \qquad 4.$$

where r is the interparticle distance, and the strength V_0 and range r_0 are useful parameters for exploring the low-energy dynamics associated with the existence of one (bound or virtual) state close to threshold. For bound states, the wave function is obtained by solving the S-wave Schrödinger equation

$$\left(\frac{\partial^2}{\partial z^2} - \frac{m r_0^2 V_0}{\hbar^2} e^{-z^2} - \frac{r_0^2}{a_B^2}\right) \phi_B(z) = 0, \qquad 5.$$

where $z = r/r_0$, and $\phi_B(z)$ is the reduced wave function. At zero energy, $r_0/a_B = 0$, and at large separation values, $\phi_0(z \to \infty) \to 1 - z r_0/a$, from which the scattering length a is extracted. The zero-energy wave function, ϕ_0, also determines the effective range, r_e. The small value of the ratio r_e/a_B can be used to characterize the unitary window, and, with the discussion limited to the case of one bound state, the energy values of a generic Gaussian potential inside the window can be organized in the single curves shown in **Figure 1*a*,*b***. In **Figure 1*a***, r_e/a_B is given as a function of r_e/a. Real systems can be placed on the figure using the corresponding values of a, a_B, and

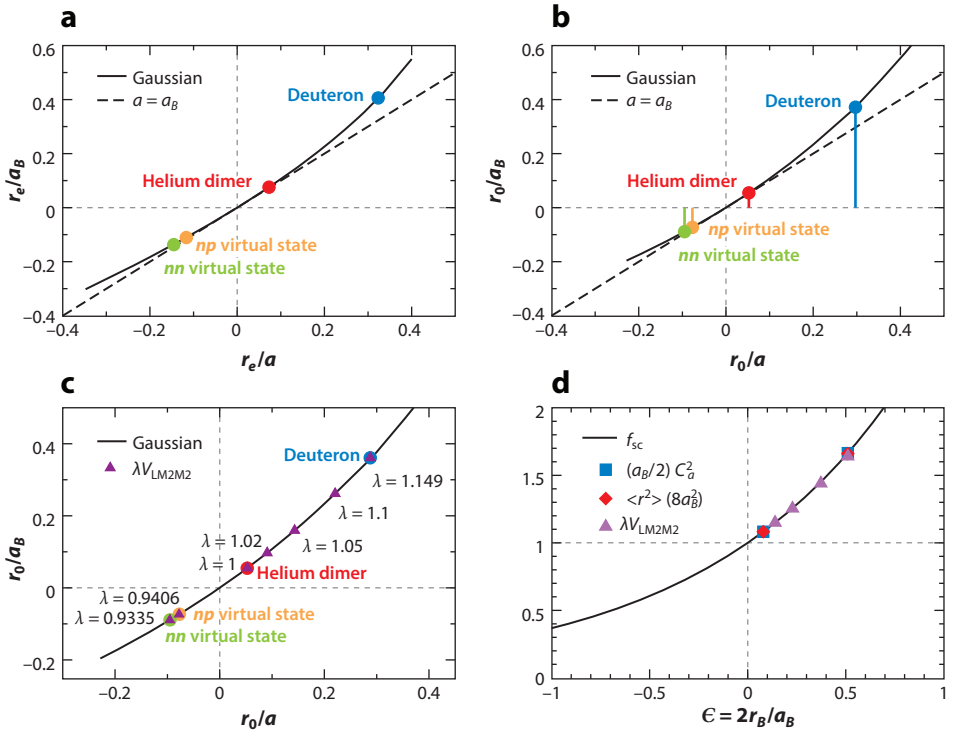

Figure 1

The inverse of the energy length as a function of the inverse of the scattering length, shown in units of (*a*) r_e and (*b*) r_0, for a Gaussian potential. Solid circles indicate the position of selected real systems. (*c*) Position of the helium dimer (*red circle*), modified helium dimers (*purple triangles*), and the two-nucleon systems (*blue*, *orange*, and *green circles*) on the Gaussian curve. (*d*) Collapse of the observables on the scaling function. The modified helium dimers are shown as purple triangles.

Table 1 Low-energy parameters of the helium dimer, calculated with the LM2M2 interaction, and those of the *np* 1^+ and 0^+ states and the *nn* 0^+ state calculated with the AV18 interaction

He dimer	E_2 (mK)	a_B (a_0)	C_a ($a_0^{-1/2}$)	$\sqrt{\langle r^2\rangle}$ (a_0)	a (a_0)	r_e (a_0)	r_0 (a_0)
LM2M2	−1.3035	182.221	0.108985	67.015	189.415	13.845	10.03
$\lambda = 1.02$	−4.0905	102.864	0.149498	38.979	110.022	13.396	9.99
$\lambda = 1.05$	−11.137	62.3388	0.200802	24.678	69.4483	12.792	9.94
$\lambda = 1.10$	−30.358	37.7585	0.277525	16.024	44.7923	11.937	9.88
$\lambda = 1.149$	−57.981	27.3217	0.349857	12.362	34.2868	11.248	9.86
NN	E_2 (MeV)	a_B (fm)	C_a ($\text{fm}^{-1/2}$)	$\sqrt{\langle r^2\rangle}$ (fm)	a (fm)	r_e (fm)	r_0 (fm)
np (1^+)	−2.2245	4.318	0.885	1.967	5.419	1.753	1.559
np (0^+)	−0.066	−25.05	—	—	−23.74	2.77	1.83
nn (0^+)	−0.102	−20.19	—	—	−18.90	2.75	1.795
He dimer	E_2 (mK)	a_B (a_0)	C_a ($a_0^{-1/2}$)	$\sqrt{\langle r^2\rangle}$ (a_0)	a (a_0)	r_e (a_0)	r_0 (a_0)
$\lambda = 0.9406$	—	−139.631	—	—	−132.318	15.445	10.19
$\lambda = 0.9335$	—	−115.147	—	—	−107.820	15.669	10.21

For the 0^+ states, the energy values are those of the virtual state. Parameters of modified helium dimers are shown as well. The values of the asymptotic normalization constant C_a and of the mean square radius are also reported.

r_e. We analyze the dimer of helium atoms and the two-nucleon system. In the case of the dimer, experimental data are not available for all those quantities, so we use values obtained with one of the most widely used helium–helium interactions, the LM2M2 potential (62). For the purposes of the present discussion, results obtained with this potential are considered equivalent to experimental data. For the two-nucleon system, we use the experimental values or, equivalently, the results of a realistic interaction, the AV18 potential (63), to determine the *np* and *nn* low-energy parameters in states $J^\pi = 1^+$ and 0^+. With the values given in **Table 1**, the deuteron, helium dimer, and *np* and *nn* states shown in **Figure 1*a*** are on top of the Gaussian curve.

In **Figure 1*b***, the plot is reformulated in terms of the Gaussian range r_0, in such a way that real systems are mapped onto the Gaussian curve through their ratio a/a_B. Their position on the curve identifies the characteristic range r_0 indicated in **Figure 1*b*** by the solid colored vertical lines. With this range, and the proper strength, a Gaussian potential simultaneously reproduces a and a_B. The characteristic ranges for the deuteron, helium dimer, and *np* and *nn* virtual states are given in **Table 1**.

2.2. Trajectories in the Universal Window

Figure 1*b* defines a Gaussian characterization of the unitary window. The position of real systems on the Gaussian curve identifies the characteristic ranges. The associated Gaussian potentials can be considered a low-energy representation of the two-body interaction of the systems. Through the variation of the Gaussian strength, a system can (ideally) be moved along the unitary window. Physical systems exist at their physical points, so the interaction has to be modified to move them from that point. At present, this can be done in the case of the residual interaction between atoms by applying magnetic fields to change their electronic structure. The difficult technical implementations of this procedure could limit the knowledge of the new interaction, allowing one only to trace a few parameters of it. We refer, for example, to the sector of trapped cold atoms in which the applied magnetic field is related to changes in the two-body scattering length. When this parameter is allowed to take large values (and eventually diverges), the system moves inside

the universal window. Since the window is characterized essentially by two parameters, a_B and a, the lack of knowledge of the complete interaction is not important; the low-energy properties of the system inside the window are determined by them. Accordingly, the characterization of the universal window by the Gaussian potential could be of interest.

To analyze possible trajectories along the unitary window, we use as an example the LM2M2 interaction of two helium atoms and define V_λ as follows:

$$V_\lambda = \lambda V_{\mathrm{LM2M2}}. \qquad 6.$$

The value $\lambda = 1$ refers to the original potential, whereas for slightly bigger and lower values of λ, the system moves along the window. The different λ values generate fictitious helium dimers mimicking possible modifications of the original potential. For selected cases of λ, the corresponding low-energy quantities are given in **Table 1** and shown in **Figure 1*c***. The two-nucleon systems are also shown on the curve, and for the given values of λ, the position of these modified helium dimers along the curve coincides in specific cases with the nuclear systems. For each case, the range of the Gaussian potential that reproduces the values of a_B and a is shown in the last column of **Table 1**. We note that the Gaussian range of the modified dimers varies little along the window; thus, it is possible to define a characteristic Gaussian range associated with the helium dimer.

The above analysis is useful for characterizing the universal behavior in terms of the position of a system inside the universal window. Similar locations inside the universal window imply similar dynamical properties. Indeed, we can use the wave function to calculate several observables, such as the mean square radius,

$$\langle r^2 \rangle = \frac{r_0^2}{4} \int_0^\infty dz\, z^2 \phi_B(z)^2 = \frac{a^2}{8} \left\{ 1 + \left(\frac{r_B}{a}\right)^2 + o\left[\left(\frac{r_B}{a}\right)^3\right] \right\} \simeq \frac{a_B^2}{8} e^{2r_B/a_B}, \qquad 7.$$

and the asymptotic normalization constant, which is defined when $\phi_B(z > 2r_B/r_0) \to C_a e^{-zr_0/a_B}$ and directly related to the residue of the S-matrix at the momentum pole $k = i/a_B$:

$$C_a^2 \simeq \frac{2}{a_B} \frac{1}{1 - r_e/a_B} = \frac{2}{a_B} e^{2r_B/a_B}. \qquad 8.$$

The above quantities explicitly depend on the two low-energy data points, and we have introduced, valid up to third order, the following scaling function:

$$f_{\mathrm{sc}} = \frac{1}{1 - r_e/a_B} = e^{2r_B/a_B}. \qquad 9.$$

Inside the universal window, observables are controlled by the large parameter a_B with corrections given by the small parameter $r_e/a_B = 2r_B/a$ or $\epsilon = 2r_B/a_B$. In the case of $\langle r^2 \rangle$ and C_a^2, this is encoded in the scaling function f_{sc}, as explicitly shown in **Figure 1*d***. The values given in **Table 1**, properly divided by the indicated factors, are located in the figure, and they are well described by the scaling function at the corresponding value of ϵ. The collapse on the curve is well verified for very different systems, in particular those close to the unitary limit. This analysis clearly shows the CSI and the universal characteristic of the window. Moreover, it shows that the dynamics is determined by the small parameter ϵ as continuously emerging from the unitary point ($\epsilon = 0$).

2.3. Correlations Inside the Universal Window

When the interaction between two particles is strongly repulsive at short distances, the two-body system is, as a consequence, highly correlated. For bound systems, the probability of being inside the repulsive core is very small. Accordingly, the wave function in that region is almost zero

and increases rapidly toward the attractive region. Therefore, the total energy results from a big cancellation between the kinetic and potential energy. Systems such as the helium dimer or the deuteron are examples of this kind of correlation. It is interesting to analyze the description of these systems in terms of the low-energy parameters. Outside the interaction region, the *S*-wave reduced wave function of the system is

$$\psi_B(r \to \infty) = C_a e^{-r/a_B}, \tag{10.}$$

and the probability P_e of being in that region is defined as

$$P_e = C_a^2 \int_{2r_B}^{\infty} e^{-2r/a_B} dr = C_a^2 \frac{a_B}{2} e^{-4r_B/a_B} = \frac{1}{1 - r_e/a_B} e^{-4r_B/a_B} = e^{-2r_B/a_B} = \frac{1}{f_{sc}}, \tag{11.}$$

where we have used Equation 8 and identified $2r_B$ as the lower limit for two particles to be considered outside the interaction region. Accordingly, P_e—the probability of being outside the interaction region—is the inverse of the scaling function. For weakly bound systems, this quantity is governed by the ratio $2r_B/a_B$; therefore, we consider the systems inside the unitary window to be strongly correlated.

3. THE THREE-BODY UNIVERSAL WINDOW

In this section, we discuss the Gaussian characterization of the universal window in the case of three equal bosons and that of three equal fermions with 1/2 spin–isospin symmetry; the latter case is of interest for nuclear physics. The three-body system inside the window has remarkable properties, most notably the Efimov effect, a manifestation of DSI that strongly constrains the three-body physics. CSI of the two-body system is broken at the level of three particles by the introduction of a new scale governed by the energy value of the three-body system at unitarity. On the one hand, these interesting properties triggered an enormous amount of experimental work regarding the behavior of three particles inside the universal window (36, 64–69). On the other hand, it is of fundamental importance to understand correlations between low-energy properties and the specific location of a system inside the window. In particular, in the case of nucleons, these correlations will be taken as signatures of universal behavior.

3.1. The Three-Boson System: Bound States

In the case of a zero-range interaction, the three-body system is unbound from below (Thomas collapse) (70). Its spectrum, deduced by Vitaly Efimov, is given by the Efimov radial law (34, 35):

$$\frac{E_3^{(n)}}{E_2} = \tan^2 \theta, \tag{12.}$$

$$E_3^{(n)} + E_2 = e^{-2(n-n_*)\pi/s_0}\, e^{\Delta(\theta)/s_0} E_*. \tag{13.}$$

For each value of the angle θ, the binding energy of level n, $E_3^{(n)}$, is determined simultaneously by the two-body binding energy, which in the zero-range limit ($a = a_B$) is $E_2 = \hbar^2/ma^2$, and by the binding energy of level n_* at the unitary limit, $E_* = \hbar^2\kappa_*^2/m$, which defines the three-body parameter κ_*. The function $\Delta(\theta)$ is a universal function (the same for all levels) that governs the values of the three-body binding energy inside the window. With the above definition, $\Delta(-\pi/2) = 1$, and parameterizations of the universal function exist (37, 44, 71) for θ varying in the range $(-\pi, -\pi/4)$. At $\theta = -\pi/2, E_2 = 0$, and the spectrum shows the Efimov effect: a geometrical tower of states with constant energy ratios $E_3^{(n)}/E_3^{(n+1)} = e^{2\pi/s_0}$, where, in the case of three equal bosons,

the universal number is $s_0 = 1.006237\ldots$. The zero-range spectrum of Equation 13 verifies the DSI: It is invariant when the scattering length a is scaled by the factor $e^{m\pi/s_0}$, where m is an integer number and both the three-body parameter κ_* and the angle θ are kept fixed.

The zero-range model can be extended to consider the finite-range character of the interaction. In this case, the Thomas collapse is no longer present, and the three-body spectrum can be written as

$$E_3^{(n)} + E_2 = e^{\Delta_3^{(n)}(\theta)/s_0} E_*^{(n)}, \qquad 14.$$

where $n = 0, 1, \ldots$ indicates the energy levels, and $\Delta_3^{(n)}$ is the n-level function defined as

$$\Delta_3^{(n)}(\theta) = s_0 \log \frac{E_3^{(n)} + E_2}{E_*^{(n)}}. \qquad 15.$$

The above n-level function depends on the particular interaction used to compute the energy values. Moreover, $E_2 = \hbar^2/ma_B^2$, and $E_*^{(n)} = \hbar^2[\kappa_*^{(n)}]^2/m$ is the energy of level n at the unitary limit, with the three-body parameter of each level defined as $\kappa_*^{(n)}$. When finite-range potentials are used to compute the n-level function, the following behavior is verified (72):

$$\Delta_3^{(n)}(\theta) \to \Delta(\theta) \qquad n > 1, \qquad 16.$$

$$\frac{E_*^{(n)}}{E_*^{(n+1)}} \to e^{2\pi/s_0} \qquad n > 1. \qquad 17.$$

Only the lowest levels, and in particular the ground state ($n = 0$), show range effects. Starting from $n = 2$, the energy spectrum closely tends toward the zero-range spectrum of Equation 13. The practical use of Equations 13 and 14 depends on knowledge of the universal and level functions $\Delta(\theta)$ and $\Delta_3^{(n)}(\theta)$, respectively. In the first case, it is possible to solve the Skorniakov–Ter–Martirosian equations (73) for different values of the two-body scattering length a to cover the region of interest given by $-\pi < \theta < -\pi/4$ (71). In the case of finite-range interactions, knowledge of the n-level function along the unitary window is related to knowledge of the interaction in that region. In general, the interaction is known at one point—the physical point—and to explore the unitary window some assumptions are needed. In many cases, scaled potentials have been used to slightly increase or reduce their strength as a way to explore the universal window; here, we use the Gaussian potential of Equation 4 as the reference interaction to characterize the universal window.

The results for a Gaussian potential of range r_0 with variable strength can be summarized in the following equations (74–77):

$$a_B\kappa_3^{(n)} = \tan\theta, \qquad 18.$$

$$r_0\kappa_3^{(n)} = \gamma_3^{(n)} e^{\Delta_3^{(n)}(\theta)/2s_0} \sin\theta, \qquad 19.$$

where $\gamma_3^{(n)} = r_0\kappa_*^{(n)}$ and $E_3^{(n)} = \hbar^2[\kappa_3^{(n)}]^2/m$. The level functions $\Delta_3^{(n)}$ are computed by solving the Schrödinger equation with a Gaussian potential with variable strength, whereas the pure numbers $r_0\kappa_*^{(n)} = \gamma_3^{(n)}$ define the three-body parameter of each level at $\theta = -\pi/2$. It should be noted that $\Delta_3^{(n)}$ and $\gamma_3^{(n)}$ are the same for all Gaussian potentials.

In **Figure 2**, the first three levels of the Gaussian potential are shown in a $(r_0/a_B)^{1/2}, -[r_0\kappa_3^{(n)}]^{1/4}$ plot. The powers 1/2 and 1/4 in the axis variables are used to make the three levels more visible.

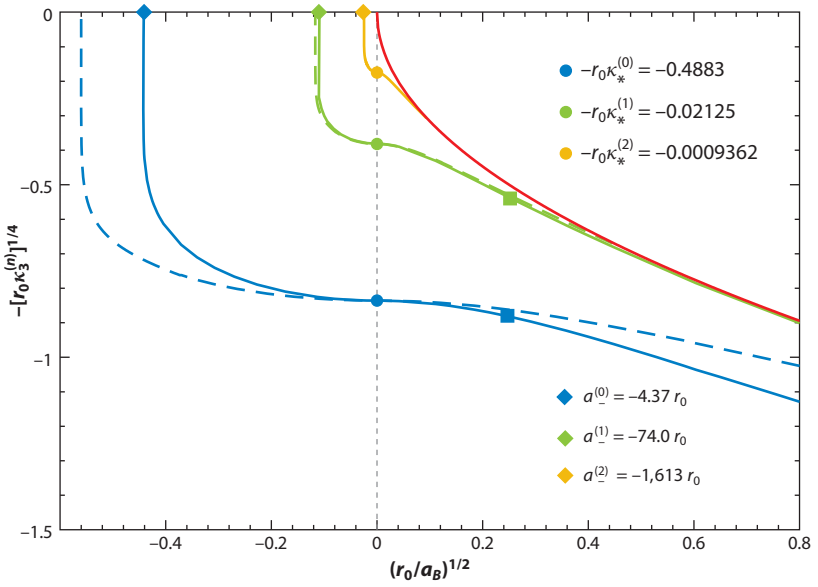

Figure 2

The dimensionless quantity $-[r_0\kappa_3^{(n)}]^{1/4}$ for $n = 0,1,2$, shown as a function of $(r_0/a_B)^{1/2}$ for a Gaussian potential (*solid lines*). The dashed lines indicate the results from the zero-range model. The red line indicates the two-body threshold. Notable values at $\theta = -\pi/2$ and $-\pi$ are shown as solid circles and diamonds, respectively. The solid squares represent the two levels of the helium trimer using the LM2M2 interaction, $E_3^{(0)} = 126.4$ mK and $E_3^{(1)} = 2.27$ mK.

The zero-range results are also shown, making the correspondence of the two models at the unitary limit. Range effects are appreciable in the ground state, very reduced in the first excited state, and almost negligible at higher levels. The solid circles on the $r_0/a_B = 0$ axis of **Figure 2** indicate the first γ_n values, whereas the points where the bound states disappear into the three-body continuum, $E_3^{(n)} = 0$, define the corresponding values of the scattering length $a_-^{(n)}$ (solid diamonds), in units of the Gaussian range. Using the values shown in **Figure 2**, the almost model-independent quantities can be extracted:

$$\kappa_*^{(0)} a_-^{(0)} = -2.14, \tag{20.}$$

$$\kappa_*^{(1)} a_-^{(1)} = -1.57, \tag{21.}$$

$$\kappa_*^{(2)} a_-^{(2)} = -1.51. \tag{22.}$$

In the case of the ground state, the estimate for van der Waals systems is $\kappa_*^{(0)} a_-^{(0)} \approx -2.2$ (see 44 and references therein). Therefore, the Gaussian characterization captures most of the ingredients of those systems inside the universal window. Moreover, in the $n = 1$ and $n = 2$ cases, the values tend rapidly toward the zero-range value of $a_-\kappa_* = 1.507$ (78).

Figure 2 also shows the two levels of the helium trimer using the LM2M2 interaction. Given that $E_2 = 1.303$ mK, the position of these data on the plot is fixed through the angle θ, which is defined as $E_3^{(n)}/E_2 = \tan^2\theta$. The axis value of $r_0/a_B = 0.061$, which corresponds to the ground state, can be used to determine the characteristic Gaussian range $r_0^{(0)} = 11.15\, a_0$ with which a

Gaussian potential reproduces the dimer and ground state trimer energies. From that value, the three-body parameters of the ground and excited states of the helium trimer can be estimated (79):

$$E_*^{(0)} = \frac{\hbar^2}{m}\left[\frac{\gamma_0}{r_0^{(0)}}\right]^2 = 83.1\,\text{mK}, \qquad 23.$$

$$E_*^{(1)} = \frac{\hbar^2}{m}\left[\frac{\gamma_1}{r_0^{(0)}}\right]^2 = 0.157\,\text{mK}, \qquad 24.$$

in complete agreement with the predictions given in the literature (80, 81). Moreover, at the three-atom continuum, the characteristic range predicts the value $a_-^{(0)} = -48.7\,a_0$, in agreement with the helium values at that point (see 80). Using the scaled van der Waals length of helium, $\tilde{r}_{\text{vdW}} = \lambda^{1/4} r_{\text{vdW}}$, the Gaussian trajectory predicts $a_-^{(0)}/\tilde{r}_{\text{vdW}} \approx -9.6$, in close agreement with the universal value observed in van der Waals species (see 44 and references therein).

3.2. The Three-Boson System: Scattering States

Considering three equal spin 0 atoms as representative of the three-boson system, the Gaussian characterization of the universal window can be applied to study the atom–dimer scattering length a_{AD}. In the zero-range limit, its expression, derived by Efimov (82), is

$$a_{AD}/a_B = d_1 + d_2 \tan[s_0 \ln(\kappa_* a_B) + d_3], \qquad 25.$$

where d_1, d_2, and d_3 are universal numbers and κ_* is the three-body parameter belonging to one of the three-body energy branches. The log-periodic functional form of the observable is a consequence of the constraints imposed by DSI. As $a_B \to \infty$, the ratio a_{AD}/a_B forms different branches with asymptotes located at values of a_B at which the three-body levels disappear into the atom–dimer continuum. In the case of finite-range interactions, we use the parameterization proposed in Reference 74,

$$a_{AD}/a_B = d_1 + d_2 \tan\{s_0 \ln[\kappa_*^{(n)} r_0 (a_B/r_0) + \Gamma_3^{(n)}] + d_3\}, \qquad 26.$$

where the pure number $\kappa_*^{(n)} r_0 = \gamma_3^{(n)}$ is used as the driving term and we have introduced the finite-range three-body parameter $\Gamma_3^{(n)}$, as discussed in References 74 and 75, to absorb finite-range corrections.

We analyze the behavior of a_{AD} inside the unitary window using a Gaussian potential. Following Reference 79, we show in **Figure 3*a*** two branches of the function a_{AD}/a_B using $\gamma_3^{(1)} = 0.02125$ as the driving term, $d_1 = 1.541$, $d_2 = -2.080$, $d_3 = -2.038$, and $\Gamma_3^{(1)} = 0.061$. **Figure 3*a*** also shows the lowest four energy levels: ground state (solid blue line) and first (solid green line), second (solid orange line), and third (solid black line) excited states. The two-body energy is represented in **Figure 3*a*** by the solid red line, and the two asymptotes (dashed black vertical lines)—extracted from Equation 26 and located at $r_0/a_B = 0.0139$ and 0.00059—indicate the positions at which the third (black circle) and second (orange circle) excited states disappear into the continuum. Also shown in **Figure 3*a*** are the positions on the characteristic Gaussian curve of the first excited state of the helium trimer at the $n = 1$ level (lower green diamond) and at the $n = 2$ level (lower orange diamond). These points correspond to the crossing of a straight line passing through the origin, defined by the angle $E_3^{(1)}/E_2 = \tan^2\theta$, with the $n = 1$ and $n = 2$ levels. For the $n = 1$ level, the value of the axis $r_0/a_B = 0.0637$ corresponds to the value $a_{AD}/a_B = 1.19$ (higher green diamond in **Figure 3*a***). Therefore, the Gaussian characterization of the unitary window predicts the atom–dimer scattering length to be $a_{AD} = 1.19\,a_B$. Using the LM2M2 value,

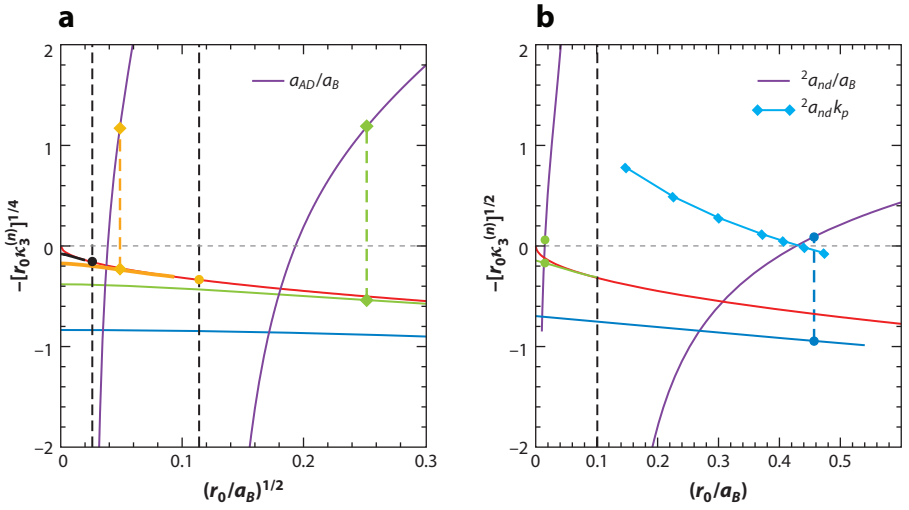

Figure 3

(*a*) The lowest four Gaussian energy levels for $N = 3$: ground state (*solid blue line*) and first (*solid green line*), second (*solid orange line*), and third (*solid black line*) excited states. The two-body energy is represented by the solid red line. The two asymptotes (*dashed black vertical lines*) indicate the positions at which the third (*black circle*) and second (*orange circle*) excited states disappear into the continuum. The positions of the first excited state of the helium trimer at the $n = 1$ level (*lower green diamond*) and at the $n = 2$ level (*lower orange diamond*) are shown too. The a_{AD}/a_B function is shown as the violet curve. The higher green and orange diamonds represent the values corresponding to the $n = 1$ and $n = 2$ levels, respectively. To guide the eye, the lower and higher diamonds are connected by orange and green vertical dashed lines. (*b*) Ground (*solid dark blue line*) and first excited (*solid green line*) states of the $J = 1/2^+$ three-nucleon system. The solid red line represents the ground state of the 1^+ two-nucleon system. The lower dark blue and green circles map the ^{3}H nucleus onto the Gaussian ground and first excited state curves, respectively. The neutron–deuteron scattering length is represented by the violet curve. The dashed black vertical line is the asymptote separating the two branches. The higher dark blue and green circles represent the values corresponding to the ground and first excited states, respectively. The solid light blue line shows the evolution of the three-nucleon virtual state. To guide the eye, the lower and higher dark blue circles are connected by a dark blue vertical dashed line.

$a_B = 182.22\, a_0$, the value $a_{AD} = 217\, a_0$ is obtained, which has to be compared with the LM2M2 value for this quantity of $218.4\, a_0$ (83). Thus, the Gaussian characterization of the universal window can accurately take into account finite-range effects. Accordingly, within an EFT we consider this result at the NLO level, in the sense that it includes range corrections.

DSI allows one to map the excited state of the trimer on a higher branch (lower orange diamond in **Figure 3*a***) corresponding to the values $r_0/a_B = 0.00239$ and $a_{AD}/a_B = 1.17$ (higher orange diamond in **Figure 3*a***). The prediction is now $a_{AD} \approx 213\, a_0$. Within an EFT, we consider this result as corresponding to the LO of the EFT, as the $n = 2$ or higher branches have almost negligible finite-range effects. This simple analysis shows the strong correlation between low-energy observables inside the unitary window. Moreover, it shows how the different branches can be used to estimate finite-range effects. Recent studies of the three-boson continuum can be found in Reference 84.

3.3. The Three-Nucleon System

The two-nucleon system in the states $J^\pi = 0^+$ and 1^+ belongs to the universal window. The 0^+ state is an *S*-wave state, whereas the 1^+ state has a dominant *S*-wave component at low energies; in

the case of the deuteron, it is about 95%. The lightest nuclei—^{2}H, ^{3}H, ^{3}He, and ^{4}He—have a high probability of being in $L = 0$, and therefore we expect to observe universal properties. Important issues to clarify are the lack of excited states in the three- and four-nucleon systems. Moreover, the doublet neutron–deuteron scattering length, ${}^2a_{nd} \approx 0.65$ fm, is very small compared with the triplet neutron–proton scattering length, $a_{np} \approx 5.2$ fm. In addition, data for low-energy neutron–deuteron scattering reveal the presence of a triton virtual state. These properties can be traced back to the position of the nuclear system inside the universal window.

The study of the universal window in the case of three nucleons has to consider the two different values of the singlet and triplet scattering lengths, a_s and a_t. Among different possibilities, we choose to maintain the ratio a_s/a_t close to the experimental value, $a_s/a_t = -4.38$, in our exploration of the unitary window (85). Therefore, the change in one value fixes the value of the other. To characterize the universal window, we construct a spin-dependent Gaussian potential with different strengths and ranges in the spin–isospin channels S, $T = 0$, 1 and 1, 0,

$$V(r) = V_0 e^{-r^2/r_0^2}\mathcal{P}_0 + V_1 e^{-r^2/r_1^2}\mathcal{P}_1, \qquad 27.$$

where $\mathcal{P}_0$ projects onto the S, $T = 0$, 1 channel and $\mathcal{P}_1$ onto the S, $T = 1$, 0 channel. Below, we study the spectrum of the three-nucleon $J^\pi = 1/2^+$ state considering $r_0 = r_1$, for which choice, at the unitary limit, the spectrum coincides with the boson case. The Gaussian strengths are varied to examine the plane $r_0/a_B, -r_0\kappa_3^{(n)}$, with $E_3^{(n)} = \hbar^2[\kappa_3^{(n)}]^2/m$ being the binding energy of level n and $E_2 = \hbar^2/ma_B^2$ the two-body binding energy of the triplet state. In **Figure 3*b***, we show the ground state ($n = 0$, solid dark blue line) and first excited state ($n = 1$, solid green line) of the $J = 1/2^+$ three-nucleon system; the solid red line indicates the ground state of the 1^+ two-nucleon system. The ^{3}H nucleus is mapped onto the Gaussian ground state curve as a dark blue circle at coordinates verifying $\kappa_3^{(0)}a_B = \tan\theta = 1.95$, which corresponds to the square root of the ratio of the triton binding energy of 8.48 MeV with the deuteron binding energy of 2.224 MeV. At that point, $r_0/a_B = 0.457$, from which the characteristic Gaussian range $r_0^{(0)} = 1.97$ fm can be estimated and used to assign a value for the three-nucleon system at unitarity through the quantity $\kappa_*^{(0)}r_0 = 0.4883$. We obtain $E_*^{(0)} \approx 2.55$ MeV in good agreement with previous estimates (22, 86).

Figure 3*b* also shows the doublet neutron–deuteron scattering length, ${}^2a_{nd}$, calculated with the Gaussian interaction, as a violet curve (in units of the energy length a_B). It corresponds to a fit of the numerical results using the form given by Equation 26 (see 79). Two branches are shown in **Figure 3*b***; the dashed black vertical line, the asymptote at $r_0/a_B = 0.101$, indicates the position at which ${}^2a_{nd}$ diverges, and the first excited state disappears into the $1 + 2$ continuum. Using the characteristic range $r_0^{(0)} = 1.97$ fm, we estimate the evaporation of the first excited state at $a_B = 18.8$ fm, which corresponds to a deuteron energy of around 0.12 MeV and a scattering length around 20 fm—very far from the corresponding physical values. This simple analysis explains the one-level structure of ^{3}H in terms of its position inside the Gaussian characterization of the unitary window. The correlation between the ground state and the doublet scattering length can be studied by looking at the value of ${}^2a_{nd}/a_B$ for $r_0/a_B = 0.457$, the coordinate of the physical point on the ground state curve. This gives ${}^2a_{nd}/a_B = 0.08$ (upper dark blue circle in **Figure 3*b***). With a deuteron energy length of $a_B = 4.32$ fm, the resulting doublet scattering length is ${}^2a_{nd} \approx 0.4$ fm. This value is slightly lower than the experimental value of 0.65 fm; however, this analysis explains the very low value of this quantity compared with that of the np triplet scattering length. We observe the very delicate region in which ${}^2a_{nd}$ is located, where slightly different values of r_0/a_B could produce large variations of ${}^2a_{nd}$, including a change of sign. The Gaussian characterization maps ${}^2a_{nd}$ in the correct (positive) region, clarifying the strong correlation between this quantity and the ^{3}H energy—a property that was already observed many years ago (87). It is possible to use the higher branch of the ${}^2a_{nd}/a_B$ curve to determine the size of finite-range corrections. The

triton point is located on the $n = 1$ level (lower green circle in **Figure 3*b***) at $r_0/a_B = 0.015$, which corresponds to ${}^2a_{nd}/a_B = 0.06$—slightly lower than the value obtained when analyzing the $n = 0$ level. As for the boson case, these two estimates can be considered in the EFT as corresponding to NLO and LO, respectively. This simple analysis explains some peculiarities of the nuclear system that are strictly correlated to its location inside the universal window.

Finally, we discuss the evolution of the three-nucleon virtual state after the $n = 1$ level crosses the $1 + 2$ continuum. Following References 79 and 88, the S-matrix energy pole $E_p = -3\hbar^2 k_p^2/4m$ is determined from the S-wave low-energy phase shifts calculated using the Gaussian potential of Equation 27. The behavior of the $a_{nd}k_p$ function is shown in **Figure 3*b*** by the solid light blue line fitting the numerical calculations (light blue diamonds). This function crosses the physical point at $r_0/a_B = 0.457$, from which the triton virtual state $E_p = 0.48$ MeV can be extracted. The Gaussian characterization explains this value in agreement with experimental determinations and theoretical investigations (50, 61, 89–92).

4. CHARACTERIZATION OF THE UNITARY WINDOW FOR MORE THAN THREE PARTICLES

The Gaussian characterization of the universal window can be extended to describe systems composed of more than three particles. DSI, which emerges in the three-body sector and gives rise to the Efimov spectrum, strongly constrains the $N > 3$ (bosons) or $A > 3$ (nucleons) energy spectrum. For equal bosons, where the spatial wave function is symmetric, DSI can be observed well beyond three particles. In the case of A nucleons, the symmetric spatial wave function is dominant only up to four particles, and deviations from the bosonic Efimov scenario appear for the $A > 4$ levels; in this case, it is interesting to explore how the energy levels emerge receding from the unitary limit.

4.1. *N*-Boson Systems

The unitary window for N bosons can be characterized using the Gaussian potential from Equation 4. Tuning the strength of the potential, one calculates the ground and excited state energies, $E_N^{(0)}$ and $E_N^{(1)}$, as functions of the two-body scattering length a, or equivalently the energy length a_B. The results of these calculations are presented in **Figure 4** for $N = 4$, 5, and 6. Results for $E_N^{(0)}$, up to $N = 70$, can be found in Reference 81. A striking feature of the $N = 4$–6 spectrum is the appearance of a twin-level structure; for a given N, there are two bound states, one deep and one shallow, below each $N - 1$ ground state. This pattern is expected to repeat itself for each three-body Efimov state if the DSI is maintained and to appear as resonances in the N-body system. Studies in the four-body system exist (94–99). The existence of the twin-level structure is not restricted to a number of particles $N \leq 6$; for the Gaussian potential, the pattern is maintained up to $N = 12$ (75, 100). For a number of particles $N > 12$, a third level appears as one consequence of the finite-range character of the force. The DSI smears out, allowing for a transition between universal and nonuniversal behavior as the study of the unitary window is extended to consider deep bound states (81). Limiting the discussion to the two-level structure, Equation 19 is extended for $N > 3$ as

$$a_B\kappa_N^{(m)} = \tan\theta, \qquad 28.$$

$$r_0\kappa_N^{(m)} = \gamma_N^{(m)} e^{\Delta_N^{(m)}(\theta)/2s_0}\sin\theta, \qquad m = 0, 1, \qquad 29.$$

where $m = 0$ is the N-body ground state and $m = 1$ is the excited state close to the $(N - 1)$-body threshold. The pure numbers $\gamma_N^{(m)} = r_0\kappa_{*,N}^{(m)}$, which determine the energies at the unitary limit,

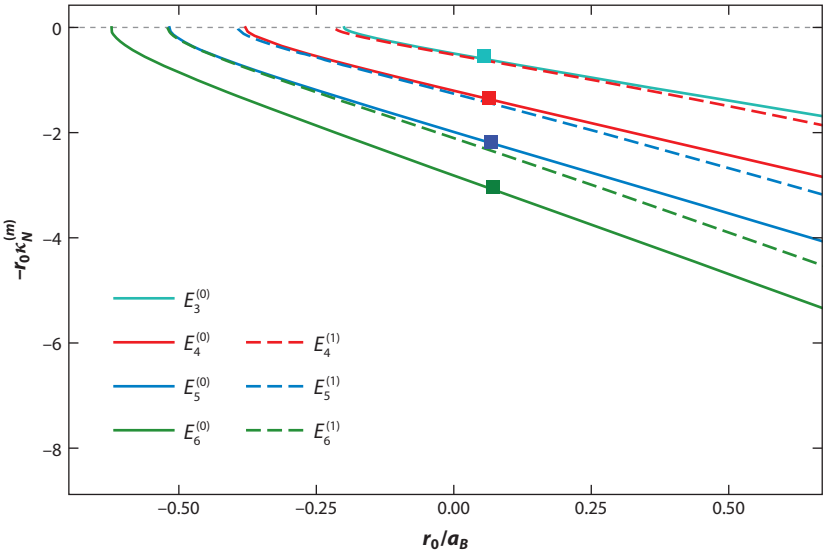

Figure 4

$N \leq 6$ energy levels given in terms of the energy momenta of the ground and excited states as functions of the inverse energy length a_B, both in units of r_0. The squares represent the ground states of the $^4\mathrm{He}_N$ clusters calculated with the realistic Tang–Toennies–Yiu (TTY) potential (93).

$E^{(m)}_{*,N}$, are characteristic of every Gaussian potential, and their values up to $N = 6$ are shown in **Table 2**. The energy of the level m is $E_N^{(m)} = \hbar^2[\kappa_N^{(m)}]^2/m$, and $\Delta_m^N(\theta)$ is the Gaussian-level function for N bosons in the states $m = 0$ and $m = 1$:

$$\Delta_N^{(m)}(\theta) = s_0 \log \frac{E_N^{(m)} + E_2}{E_{*,N}^{(m)}}. \qquad 30.$$

In the $N = 4$ case, $\Delta_4^{(m)}(\theta)$ is explicitly given in Reference 72, where it is compared to the zero-range four-body universal function. To provide evidence for the DSI character of the N-boson system, many efforts have been done to determine universal ratios between the N-body bound state energies at the unitary point in the limit of zero-range interaction. Precise numbers exist for $N = 4$ (94), whereas estimates exist for higher systems (38, 101–104). The Gaussian ratios $\gamma_N^{(0)}/\gamma_N^{(1)}$ and $\gamma_{N+1}^{(m)}/\gamma_N^{(m)}$ can be inferred from the values in **Table 2**.

To illustrate the effectiveness of the Gaussian characterization, we analyze $^4\mathrm{He}_N$ clusters, which have largely been studied with realistic helium–helium interactions (93, 105). We map these

Table 2 Gaussian pure numbers $r_0\kappa_{*,N}^{(m)} = \gamma_N^{(m)}$ ($m = 0$ and 1) at unitarity and the characteristic range and energies at the unitary limit for bosonic helium and four nucleons

	$\gamma_N^{(0)}$	$\gamma_N^{(1)}$	$r_N^{(0)}$	$E_{*,N}^{(0)}$	$E_{*,N}^{(1)}$	$E_{*,N}^{(0)}$ (HFD-HE2)
Bosonic helium						
$N = 4$	1.1847	0.512	11.85 a_0	0.433 K	0.081 K	0.440 K
$N = 5$	1.955	1.240	12.50 a_0	1.059 K	0.426 K	1.076 K
$N = 6$	2.770	2.067	13.13 a_0	1.926 K	1.073 K	1.946 K
Four nucleons	1.1847	0.512	2.078 fm	13.47 MeV	2.52 MeV	—

For bosonic helium, the results using the rescaled HFD-HE2 potential at the unitary limit are shown in the last column.

systems onto the Gaussian curves in **Figure 4** using the energies calculated in Reference 93. The position on the Gaussian curve fixes the ground state characteristic radius $r_N^{(0)}$ for each N-body system; it can be used to predict the energy of the ground and excited states of the clusters at the unitary limit. The corresponding results are given in **Table 2**. For the sake of comparison, the results of the helium–helium potential HFD-HE2 (106), rescaled at the unitary limit as discussed in Reference 81, are shown in the last column. A remarkable agreement (better than 2%) is obtained.

In general, knowledge of the $N = 2$–6 energy values of a system belonging to the universal window allows us to construct a low-energy representation of the interaction that can be used to predict the ground state energy per particle, $E_N^{(0)}/N$, of the homogeneous system. A strict correlation between the low-energy dynamics of the few-body system and the many-body system, induced from the position of the system inside the universal window, exists (81, 107–112).

4.2. Collapse of Finite-Range Interactions onto the Zero-Range Model

We make one more step in the study of universal behavior of real systems located inside the unitary window and show that the curves describing the N-body energies as functions of the energy length for different numbers of particles are actually the same curve. This is a manifestation of the strong constraints imposed by DSI and controlled by the three-body parameter (108). Following References 74, 76, and 113, the Efimov radial law, extended in Equations 19 and 29 to describe finite-range interactions, can be related to the three-body universal function by the introduction of the N-body finite-range parameter $\Gamma_N^{(n)}$ at different branches. In the specific case of $N = 3$, Equation 19 is modified by explicitly relating the finite-range spectrum to the zero-range universal function $\Delta(\theta)$ as follows:

$$\kappa_3^{(n)} a_B = \tan\theta, \quad \kappa_*^{(n)} a_B + \Gamma_3^{(n)} = \frac{e^{-\Delta(\theta)/2s_0}}{\cos\theta}, \qquad 31.$$

the origin of which has been traced to the running of the three-body scale (71, 114). What is unraveled is that each N-body system, in the ground state and in the first excited state, has its finite-range parameter $\Gamma_N^{(0)}$ and $\Gamma_N^{(1)}$, so that Equation 29 is modified as

$$\kappa_N^{(m)} a_B = \tan\theta, \quad \kappa_{*,N}^{(m)} a_B + \Gamma_N^{(m)} = \frac{e^{-\Delta(\theta)/2s_0}}{\cos\theta}, \qquad 32.$$

explicitly relating the description of the ground ($m = 0$) and excited ($m = 1$) states to the three-body universal function. In **Figure 5**, we see that the finite-range parameter $\Gamma_N^{(m)}$, which encodes the finite-range corrections, can be used to collapse the ground and excited states of the few-body systems on the three-body universal curve given by the Efimov radial law in Equation 13. This is a clear sign that these systems belong to the same universality class and that their spectra are constrained by a DSI governed by the three-body parameter $\kappa_*^{(0)}$.

4.3. The $A \leq 6$ Universal Window

In Section 3, we have discussed the universal character of the three-nucleon low-energy spectrum showing the existence of strong correlations between observables related to the position of the two- and three-nucleon systems inside the universal window. These properties suggest the possibility of describing nuclear physics as continuously linked to the unitary limit (20, 115–117). Here, we show the $A = 4$ and $A = 6$, $L = 0$ nuclear spectrum along the nuclear cut $a_s/a_t = -4.38$ using the Gaussian two-channel potential of Equation 27. **Figure 6*a*** shows the $A = 2$–4 spectrum (the Coulomb interaction is not taken into account). The 2 three-nucleon states, ^{3}H and ^{3}He, are degenerate; moreover, there is an infinite tower of excited states at unitarity as in the boson case. As the value of r_0/a_B increases, the excited states disappear one by one, and the last one, indicated

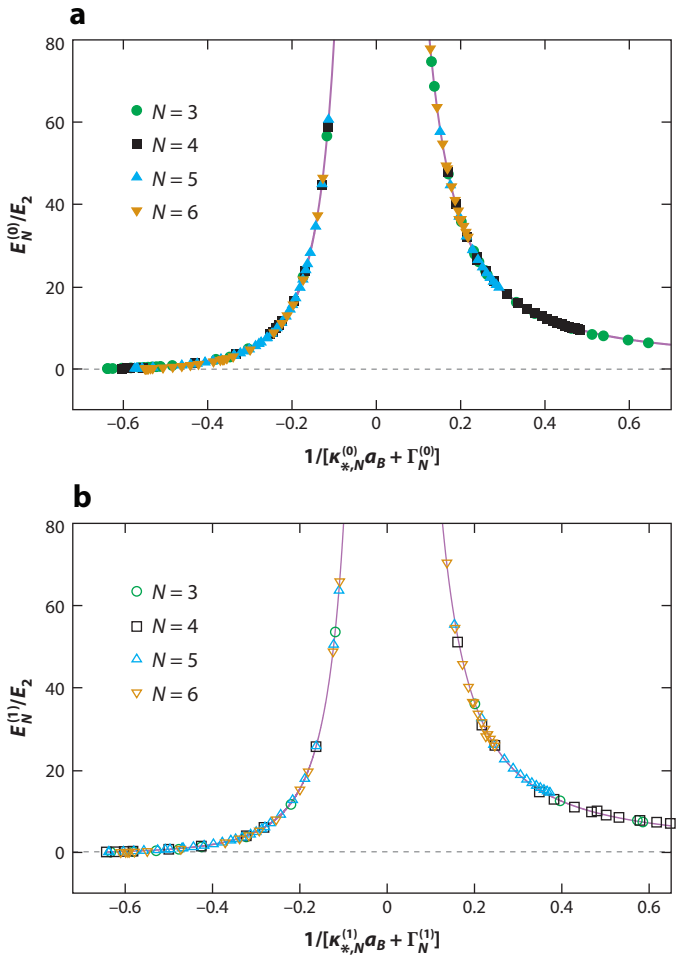

Figure 5

The (*a*) *N*-boson ground and (*b*) first excited binding energies, $E_N^{(0)}$ and $E_N^{(1)}$, in units of E_2 as a function of the inverse of the energy length a_B, in units of the *N*-body parameter $\kappa_{*,N}^{(m)}$ shifted by the finite-range parameter $\Gamma_N^{(m)}$. Different symbols represent results obtained with the Pöschl–Teller and Gaussian potential models. Figure adapted with permission from Reference 76.

in the figure as ^{3}H*, disappears at $r_0/a_B = 0.101$, resulting in the observed one-level structure of ^{3}H. The four-body spectrum has similar behavior to the bosonic case: It has a two-level structure, a deep state corresponding to ^{4}He, and one excited state, ^{4}He*, close to the three-body threshold. It should be noticed that this resonance state becomes bound without considering the Coulomb interaction (86). The ^{3}H and ^{4}He nuclei can be mapped onto the Gaussian curves through the angles defined by the corresponding energy ratios, E_3/E_2 and E_4/E_2. They are indicated in **Figure 6*a*** by the green solid square (^{3}H) and the red solid square (^{4}He). In the ^{4}He case, the binding energy should be taken as $E_4 = 29.1$ MeV, without considering the Coulomb contribution (118). Its position on the plot corresponds to a characteristic Gaussian range, $r_0^{(0)} = 2.078$ fm, from which the binding energies at unitarity, $E_{*,4}^{(0)}$ and $E_{*,4}^{(1)}$, can be deduced. They are reported in **Table 2**.

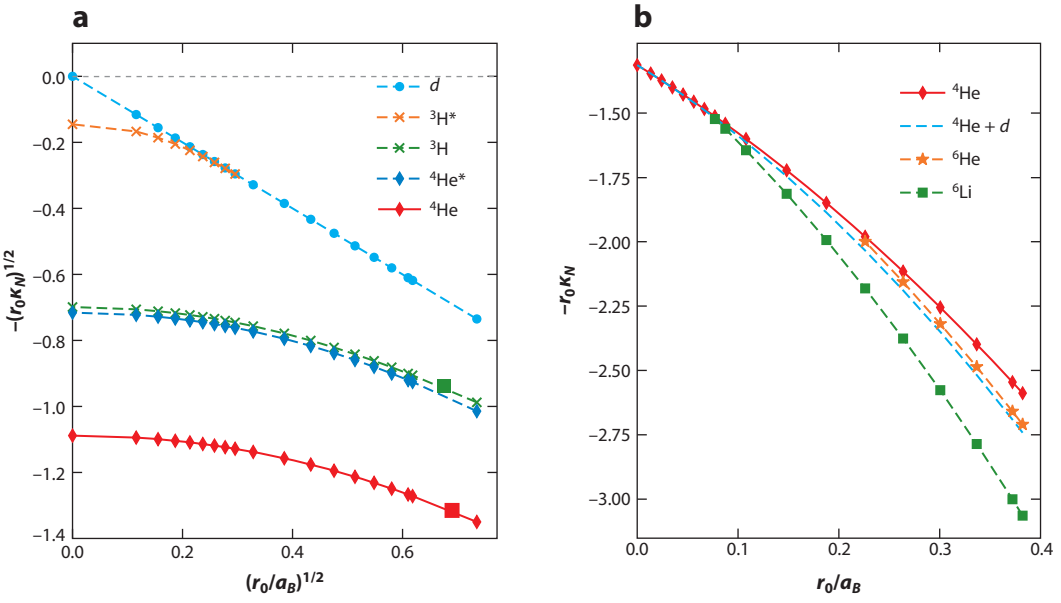

Figure 6

(*a*) Square root of the binding momenta κ_2, $\kappa_3^{(n)}$, and $\kappa_4^{(m)}$ for d, ^{3}H (and its first excited state ^{3}H*), and ^{4}He (and its first excited state ^{4}He*), respectively, along the nuclear cut $a_s/a_t = -4.3$ in terms of the inverse of the energy length a_B, both in units of the Gaussian range r_0. The positions of ^{3}H and ^{4}He at the physical point are given as green and red solid squares, respectively. (*b*) Binding momentum along the nuclear cut for $A = 6$ as a function of a_B, both in units of r_0. In both panels, the Coulomb interaction has not been taken into account. Figure adapted with permission from Reference 86.

The spectrum of the $A = 6$ systems along the nuclear cut is reported in **Figure 6*b***. There are two different $A = 6$ states discriminated by their spin–isospin quantum numbers: the ^{6}He with $S = 0$, $T = 1$, and the ^{6}Li with $S = 1$, $T = 0$. Interestingly, neither is present at the unitary limit, being above the corresponding thresholds ^{4}He and ^{4}He+d, respectively. As r_0/a_B moves toward positive values, these states emerge from their thresholds—first ^{6}Li at $r_0/a_B = 0.07$ and then ^{6}He at $r_0/a_B = 0.19$. At the physical point, the light nuclear spectrum (without considering the Coulomb interaction) consists of one level for ^{3}H and ^{3}He (which are degenerated), two levels for ^{4}He, and one level for ^{6}He and ^{6}Li. The evolution of the excited ^{4}He state with the Coulomb interaction taken into account is discussed in Section 5.2. The present analysis gives a simple explanation of the light nuclear spectrum as emerging continuously from the unitary limit.

5. IMPLICATIONS OF EFIMOV PHYSICS IN DETERMINING THE NUCLEAR EFFECTIVE FIELD THEORY

The Gaussian characterization of physical systems in the Efimov window corresponds to a regularized version of the LO EFT description, where the Gaussian range is the inverse of the ultraviolet cutoff. In this formulation, finite-range effects are implicitly contained in the cutoff and disappear as the latter is removed, recovering a scale-invariant description. Even in this limit, a scale nevertheless has to be introduced at the three-body level in the form of a dimensionful three-body parameter (37, 44); as a matter of fact, the short-distance two-body dynamics does not decouple in the three-body sector and manifests itself as an additional three-body interaction in the LO EFT designed to absorb all the cutoff dependence in the zero-range limit. By specifying the corresponding strength through a three-body datum, CSI is broken into DSI.

The sensitivity of the three-body system to the short-distance two-body dynamics depends solely on the proximity to the unitary limit and persists after the inclusion of finite-range effects (119). In particular, it applies if the EFT is interpreted as a finite-cutoff effective theory à la Lepage (120, 121), where the renormalization is done implicitly through the fitting of low-energy constants, and cutoff independence is attained only up to neglected higher orders. With a finite cutoff, the Thomas collapse is avoided and there is a well-defined three-body ground state as well as, close to unitarity, all the higher Efimov states, as exemplified in **Figure 2**. In this perspective, the cutoff is interpreted as a physical parameter related to the intrinsic scale of the theory, and therefore it is bound to assume values inside a given natural range. This constraint also identifies the spectrum of three-body bound states as a function of the two-body scattering length, or alternatively of the two-body binding energy. Variations of the cutoff within the natural range induce drastic changes in the three-body spectrum, the more so the closer the system is to the unitary limit, due to the existence of densely spaced Efimov states. Thus, close to the unitary limit, the extreme sensitivity to the cutoff also affects the finite-cutoff theory because of the strong correlations between the ground state and the other bound states, reflecting the remaining DSI. The sensitivity also concerns the continuum states, as exemplified in **Figure 3**, where one can verify that small changes in r_0 produce a change of sign in the scattering length. The introduction of an LO three-body force allows one to correctly set the three-body ground state energy, bringing the lowest branch of the Efimov plot to the curve that follows the evolution of the physical state to the unitary limit.

In other words, without a three-body force at LO, the scale of the three-body ground state is a cutoff effect, and as such it is affected by a sizeable uncertainty. Close to the unitary limit, this uncertainty would propagate to the entire tower of Efimov states, resulting in a very poor description of the shallowest ones. Thus, the EFT would be totally unable to describe those states that should, on the contrary, better fit in the domain of applicability of the EFT. The intrinsic length scale of the underlying interaction can be reconstructed by locating the systems on the universal curves through the value of the corresponding Gaussian range r_0. For example, an N-body physical system, having energy $E_N^{(0)}$, is mapped onto the Gaussian characterization of the universal window through the energy ratio $E_N^{(0)}/E_2$, where E_2 is the energy of the corresponding two-body system. With the discussion limited to equal particles and a single two-body energy level, this procedure is unambiguous. The position of the system fixes the characteristic radius $r_N^{(0)}$ with which a Gaussian potential with variable strength describes a path linking the physical point, determined by E_2 and $E_N^{(0)}$, to the unitary point, determined by $E_2 = 0$ and $E_{*,N}^{(0)} = [\gamma_N^{(0)}]^2\hbar^2/m[r_N^{(0)}]^2$. Considering different values of N of the same physical system, different characteristic ranges are obtained, as shown in **Figures 4** and **6**. Though these different Gaussian potentials are useful in determining the paths to the unitary limit, they define different potentials in each N-body sector, with different ranges all having the same order of magnitude.

By introducing a three-body force at LO, all these different descriptions can be unified as deriving from a single underlying effective Lagrangian comprising two- and three-body contact interactions (119).

5.1. The Nuclear Physical Point

The great complexity of QCD interactions produces disparate phenomena at various scales. In the chiral limit, spontaneous chiral symmetry breaking takes place and leads to the emergence of long-range collective modes, the Goldstone bosons, represented by the pions. Thus, the chiral limit defines a critical point. Since chiral symmetry is only approximate, the pions acquire a mass, but they keep their Goldstone bosons' character in that their interactions are weak at

low energies. In turn, the perturbative approach to nuclear interactions known as chiral EFT (ChEFT) is enabled (13–18, 122–124). Within this approach, the three-nucleon interaction is only a small perturbation that arises at the third order of the perturbative scheme.

Although not as directly linked to the QCD parameters as the chiral limit, another critical point can be identified in the parameter space corresponding to the unitary limit. In this case, the separation of scales is provided by the large scattering lengths, resulting in a different (pionless) EFT (24, 27–29). The two low-energy expansion schemes are different. In particular, for the reasons explained above, in the pionless EFT the three-nucleon force is part of the LO description.

The actual importance of the three-nucleon force depends on which of the two critical points can be considered closer to the physical point. Furthermore, while the chiral regime of very small quark masses is outside the Efimov window, because the scattering lengths are natural in that limit (125), the unitary regime is met for values of the pion mass around 200 MeV (22, 23), where ChEFT should still apply. Thus, the ChEFT treatment of the three-nucleon force might have to be modified accordingly by promoting it to LO, as required by Efimov physics (119). Indeed, although formally consistent, the ChEFT expansion scheme would fail in reproducing the universal correlations that arise at the unitary limit unless very high orders in the low-energy expansion were reached, so as to include the needed three-nucleon force.

To study the impact of the explicit inclusion of the pion-range interactions on the sensitivity to the short-distance dynamics that was discussed previously, we make use of the following LO Hamiltonian (119):

$$H_{\rm LO} = T + \sum_{i<j} \left[V_{\rm sr}(i,j) + V_\pi(i,j) + V_{\rm EM}(i,j) \right] + \sum_{i<j<k} W(i,j,k), \qquad 33.$$

where T is the kinetic energy, $V_{\rm sr}$ is the (regularized) short-range interaction introduced in Equation 27, $V_{\rm EM}$ is the electromagnetic interaction, and V_π is the OPEP,

$$V_\pi(r) = \boldsymbol{\tau}_1 \cdot \boldsymbol{\tau}_2 \left[\boldsymbol{\sigma}_1 \cdot \boldsymbol{\sigma}_2 Y_\beta(r) + S_{12} T_\beta(r) \right], \qquad 34.$$

with the regularized factors ($x = m_\pi r$)

$$Y_\beta(x) = \frac{g_A^2 m_\pi^3}{12\pi F_\pi^2} \frac{e^{-x}}{x} \left(1 - e^{-r^2/\beta^2} \right), \qquad 35.$$

$$T_\beta(x) = \frac{g_A^2 m_\pi^3}{12\pi F_\pi^2} \frac{e^{-x}}{x} \left(1 + \frac{3}{x} + \frac{3}{x^2} \right) \left(1 - e^{-r^2/\beta^2} \right)^2. \qquad 36.$$

Here $m_\pi = 138.03$ MeV is the average pion mass, $g_A = 1.29$ is the nucleon axial coupling constant, and $F_\pi = 2 f_\pi = 184.80$ MeV is the pion decay constant. The regularization parameter β is used to smoothly relate the chiral LO Hamiltonian to the pionless ($\beta \to \infty$) LO Hamiltonian. Moreover, $H_{\rm LO}$ includes a three-body term of the form

$$W(i,j,k) = W_0 e^{-r_{ij}^2/r_3^2} e^{-r_{ik}^2/r_3^2}, \qquad 37.$$

where r_3 is the three-body range, $r_{ij} = |\boldsymbol{r}_i - \boldsymbol{r}_j|$, and the sum in Equation 33 includes cyclic permutations of the three particles.

5.2. The Excited 0^+ State of ^{4}He

As a first application of the pionless LO Hamiltonian, we study the evolution of the ^{4}He excited state as the Coulomb interaction is adiabatically turned on, by considering $V_{\rm EM} = \epsilon e^2/r$. The parameters of the two-body potential are fixed to reproduce the *np* scattering length and effective

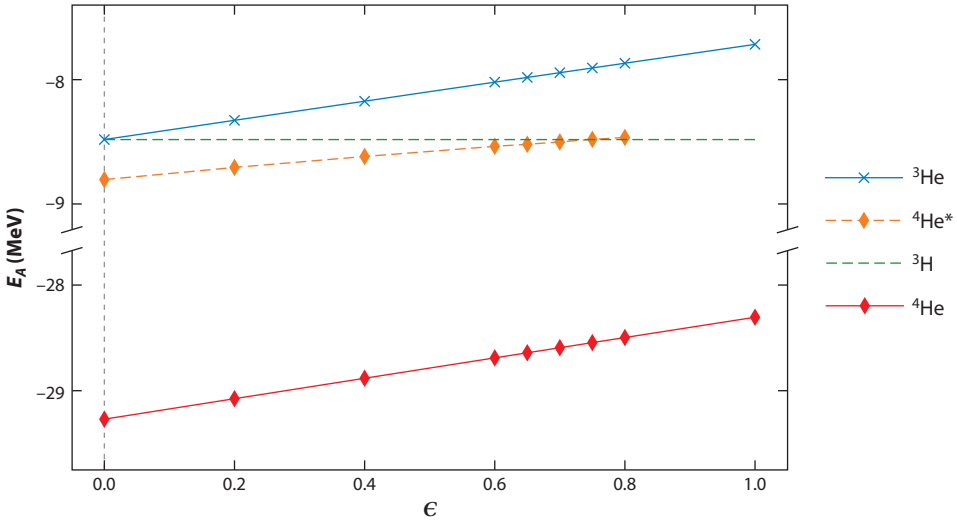

Figure 7

Evolution of the $A = 3$ and $A = 4$ energies as a function of a smooth switching-on of the Coulomb interaction via the multiplicative parameter ϵ. The full Coulomb interaction corresponds to $\epsilon = 1$. The four-body excited state, ^{4}He*, disappears at the critical value $\epsilon^* = 0.754$. At $\epsilon = 1$, the experimental energies of ^{3}H, ^{3}He, and ^{4}He are reproduced within 1% accuracy. Figure adapted with permission from Reference 86.

range in the channels S, $T = 0$, 1 and 1,0, whereas the three-body term is fixed to describe the binding energy of ^{3}H. Varying smoothly ϵ from 0 to 1, the two-body potential does not change. At the same time, the strength of the three-body force is tuned to reproduce the triton energy at each step, keeping its range fixed. The results are shown in **Figure 7**, where, for $\epsilon = 0$, we observe one $A = 3$ state and the two $A = 4$ states (38, 86, 96, 98, 103, 126). As the value of the Coulomb interaction grows to its full value, $\epsilon = 1$, the degeneracy between the ^{3}H and ^{3}He is removed and the values of the ground and excited state energies of ^{4}He change. For $\epsilon \approx 0.75$, the ^{4}He excited state disappears onto the ^{3}H+p threshold; a polynomial fit gives the critical value at $\epsilon^* = 0.754$. At $\epsilon = 1$, the correct low-energy three- and four-nucleon spectrum is recovered (86).

5.3. The Saturation Point of Nuclear Matter

The application of the $H_{\rm LO}$ from Equation 33 to the case of $A = 3$ and $A = 4$ and nuclear matter is extensively discussed in References 119 and 127. The energy per nucleon of nuclear matter is calculated using the Brueckner–Bethe–Goldstone quantum many-body theory in the Brueckner–Hartree–Fock approximation (see, e.g., 128–130 and references therein). In the calculations, the three-nucleon force has been reduced to an effective, density-dependent two-body force by averaging over the coordinates of the third nucleon (129).

The energy per particle (E/A) of symmetric nuclear matter (SNM) is shown in **Figure 8** for various parameterizations of the two- and three-body forces. In each panel, for a fixed value of the OPEP regulator β of the two-body force, the saturation curve (i.e., E/A as a function of the nucleonic density ρ) of SNM is shown using four different values of the three-nucleon force range r_3, determined to describe the ^{3}H binding energy. The empirical saturation point of SNM ($\rho_0 = 0.16 \pm 0.01$ fm^{-3}, $E/A|_{\rho_0} = -16.0 \pm 1.0$ MeV) is shown in each panel of **Figure 8**. Interestingly, the saturation point is well described for values of r_3 that are compatible with a correct description

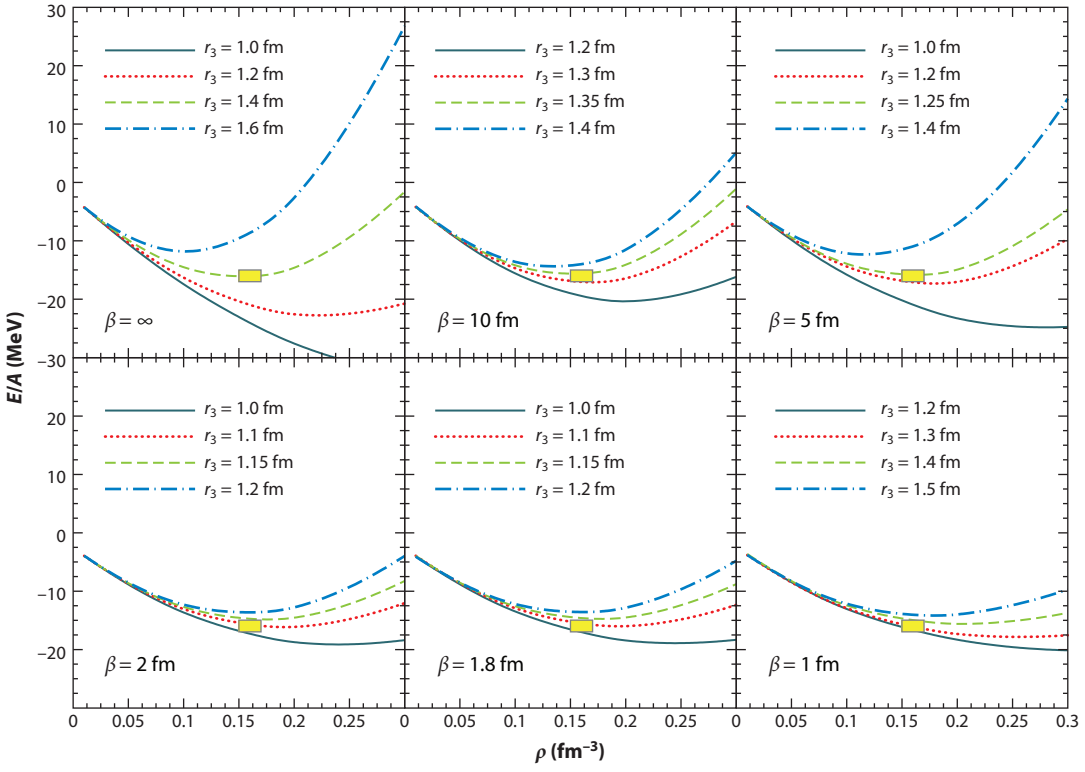

Figure 8

Energy per particle (E/A) of symmetric nuclear matter as a function of the nucleonic density ρ for several combinations of the leading order two- and three-body interactions. In each panel, the yellow box denotes the empirical saturation point. Figure adapted with permission from Reference 127.

of ^{4}He, with the best description obtained in the pionless case, $\beta \to \infty$. This is another example of strict correlations, in this case for the nuclear system, between the low-energy few-body properties and the many-body system, which are induced by the physics of the universal window.

6. SUMMARY

The Gaussian characterization of the universal window discussed in this article is based on the simplest description of the one-level two-body S-matrix (131, 132),

$$S(k) = \frac{k + i/a_B}{k - i/a_B}\frac{k + i/r_B}{k - i/r_B}, \qquad 38.$$

which is equivalent to the ERE of Equation 1. Inside the window defined by the condition $r_B \ll a_B$, we have selected a Gaussian potential to reproduce this behavior in the two-body sector and used it to extend the description to larger systems.

Two-body systems manifest CSI, depicted in **Figure 1**, which is broken into DSI in three-body systems. The procedure based on the Gaussian characterization allows one to address the impact of finite-range corrections on three-body levels. Interestingly, only the first two levels are affected in a significant way, and the higher levels tend rapidly toward the zero-range limit. The position of a physical system on the lowest level is controlled by a three-body datum. Then its spectrum and correlations with the low-energy scattering states are completely determined. Examples have

been shown for two very different systems: the helium trimer and the three-nucleon system. Furthermore, such work has been extended to larger systems in order to show to which extent they are still constrained by DSI.

We have highlighted a number of properties for systems belonging to the universal window that can be understood as consequences of their position inside the window. The present analysis suggests that the EFT describing nuclear interactions should incorporate a three-nucleon term at LO regardless of whether the pions are integrated out. This important consequence is based on the extreme sensitivity of the three-nucleon system to the cutoff effects at LO. The inclusion of a three-nucleon force at LO in the nuclear Hamiltonian will have significant consequences on the description of nuclei using precise interactions derived from ChEFT (119, 123, 124, 133, 134).

As the Gaussian characterization is used to describe systems with a larger number of particles, system-specific nonuniversal behavior starts to emerge (81, 107). Indeed, the position of a system inside the universal window determines the two-body Gaussian potential from the values of a_B and a, whereas the three-body binding energy determines the strength of the three-body potential. The use of this two- plus three-body potential to describe heavier systems introduces a dependence on a short-range scale, which is a nonuniversal effect. This effect can be incorporated by tuning the range of the three-body interaction, a parameter that can be used to improve the convergence of the EFT expansion, or by including higher orders.

Efimov physics has substantial implications for the dynamical description of systems located inside the universal window. These systems are strongly constrained by an (approximate) scale invariance. A thorough analysis of its consequences in the many-body sector is an important task that is being intensively pursued.

DISCLOSURE STATEMENT

The authors are not aware of any affiliations, memberships, funding, or financial holdings that might be perceived as affecting the objectivity of this review.

LITERATURE CITED

1. Chin C, Grimm R, Julienne P, Tiesinga E. *Rev. Mod. Phys.* 82:1225 (2010)
2. Luo F, et al. *J. Chem. Phys.* 98:3564 (1993)
3. Beane SR, Bedaque PF, Orginos K, Savage MJ. *Phys. Rev. Lett.* 97:012001 (2006)
4. Ishii N, Aoki S, Hatsuda T. *Phys. Rev. Lett.* 99:022001 (2007)
5. Yamazaki T, Ishikawa K-i, Kuramashi Y, Ukawa A. *Phys. Rev. D* 92:014501 (2015)
6. Aoki S, et al. *Prog. Theor. Exp. Phys.* 2012:1A105 (2012)
7. Beane S, Detmold W, Orginos K, Savage M. *Prog. Part. Nucl. Phys.* 66:1 (2011)
8. Weinberg S. *Phys. Lett. B* 251:288 (1990)
9. Weinberg S. *Nucl. Phys. B* 363:3 (1991)
10. Ordóñez C, van Kolck U. *Phys. Lett. B* 291:459 (1992)
11. Ordóñez C, Ray L, van Kolck U. *Phys. Rev. Lett.* 72:1982 (1994)
12. van Kolck U. *Phys. Rev. C* 49:2932 (1994)
13. van Kolck U. *Prog. Part. Nucl. Phys.* 43:337 (1999)
14. Bedaque PF, van Kolck U. *Annu. Rev. Nucl. Part. Sci.* 52:339 (2002)
15. Epelbaum E. *Prog. Part. Nucl. Phys.* 57:654 (2006)
16. Epelbaum E, Hammer HW, Meißner UG. *Rev. Mod. Phys.* 81:1773 (2009)
17. Machleidt R, Entem DR. *Phys. Rep.* 503:1 (2011)
18. Hammer HW, König S, van Kolck U. *Rev. Mod. Phys.* 92:025004 (2020)
19. Braaten E, Hammer HW. *Phys. Rev. Lett.* 91:102002 (2003)
20. König S, Grießhammer HW, Hammer HW, van Kolck U. *Phys. Rev. Lett.* 118:202501 (2017)

21. Gell-Mann M, Oakes RJ, Renner B. *Phys. Rev.* 175:2195 (1968)
22. Epelbaum E, Hammer HW, Meißner UG, Nogga A. *Eur. Phys. J. C* 48:169 (2006)
23. Beane S, Bedaque P, Savage M, van Kolck U. *Nucl. Phys. A* 700:377 (2002)
24. van Kolck U. *Nucl. Phys. A* 645:273 (1999)
25. Bedaque P, Hammer HW, van Kolck U. *Phys. Rev. Lett.* 82:463 (1999)
26. Bedaque PF, Hammer HW, van Kolck U. *Nucl. Phys. A* 646:444 (1999)
27. Kaplan DB, Savage MJ, Wise MB. *Phys. Lett. B* 424:390 (1998)
28. Birse MC, McGovern JA, Richardson KG. *Phys. Lett. B* 464:169 (1999)
29. Chen JW, Rupak G, Savage MJ. *Nucl. Phys. A* 653:386 (1999)
30. Epelbaum E, Gegelia J, Meißner UG. *Nucl. Phys. B* 925:161 (2017)
31. Epelbaum E, Gegelia J, Meißner UG. *Commun. Theor. Phys.* 69:303 (2018)
32. Grießhammer HW. *Nucl. Phys. A* 760:110 (2005)
33. Bethe HA. *Phys. Rev.* 76:38 (1949)
34. Efimov V. *Phys. Lett. B* 33:563 (1970)
35. Efimov V. *Sov. J. Nucl. Phys.* 12:589 (1971)
36. Kraemer T, et al. *Nature* 440:315 (2006)
37. Braaten E, Hammer HW. *Phys. Rep.* 428:259 (2006)
38. Hammer HW, Platter L. *Eur. Phys. J. A* 32:113 (2007)
39. Platter L. *Few-Body Syst.* 46:139 (2009)
40. Ferlaino F, Grimm R. *Physics* 3:9 (2010)
41. Ferlaino F, et al. *Few-Body Syst.* 51:113 (2011)
42. Frederico T, et al. *Few-Body Syst.* 51:87 (2011)
43. Greene CH, Giannakeas P, Pérez-Ríos J. *Rev. Mod. Phys.* 89:035006 (2017)
44. Naidon P, Endo S. *Rep. Prog. Phys.* 80:056001 (2017)
45. Zinner NT, Jensen AS. *J. Phys. G* 40:053101 (2013)
46. Marqués FM, et al. *Phys. Rev. C* 65:044006 (2002)
47. Kisamori K, et al. *Phys. Rev. Lett.* 116:052501 (2016)
48. Deltuva A. *Phys. Lett. B* 782:238 (2018)
49. Higgins MD, Greene CH, Kievsky A, Viviani M. *Phys. Rev. Lett.* 125:052051 (2020)
50. Yamashita M, Frederico T, Tomio L. *Phys. Lett. B* 670:49 (2008)
51. Frederico T, Delfino A, Tomio L, Yamashita M. *Prog. Part. Nucl. Phys.* 67:939 (2012)
52. Jensen AS, Riisager K, Fedorov DV, Garrido E. *Rev. Mod. Phys.* 76:215 (2004)
53. Hammer HW, Ji C, Phillips DR. *J. Phys. G* 44:103002 (2017)
54. Hove D, et al. *Phys. Rev. Lett.* 120:052502 (2018)
55. Kievsky A, Marcucci LE, Rosati S, Viviani M. *Few-Body Syst.* 22:1 (1997)
56. Kievsky A, et al. *J. Phys. G* 35:063101 (2008)
57. Gattobigio M, Kievsky A, Viviani M, Barletta P. *Phys. Rev. A* 79:032513 (2009)
58. Gattobigio M, Kievsky A, Viviani M, Barletta P. *Few-Body Syst.* 45:127 (2009)
59. Varga K, Suzuki Y. *Phys. Rev. C* 52:2885 (1995)
60. Bargmann V. *Rev. Mod. Phys.* 21:488 (1949)
61. Babenko V, Petrov N. *Phys. At. Nucl.* 71:50 (2008)
62. Aziz RA, Slaman MJ. *J. Chem. Phys.* 94:8047 (1991)
63. Wiringa RB, Stoks VGJ, Schiavilla R. *Phys. Rev. C* 51:38 (1995)
64. Grisenti R, et al. *Phys. Rev. Lett.* 85:2284 (2000)
65. Zaccanti M, et al. *Nat. Phys.* 5:586 (2009)
66. Berninger M, et al. *Phys. Rev. Lett.* 107:120401 (2011)
67. Machtey O, Shotan Z, Gross N, Khaykovich L. *Phys. Rev. Lett.* 108:210406 (2012)
68. Roy S, et al. *Phys. Rev. Lett.* 111:053202 (2013)
69. Klauss CE, et al. *Phys. Rev. Lett.* 119:143401 (2017)
70. Thomas LH. *Phys. Rev.* 47:903 (1935)
71. Gattobigio M, Göbel M, Hammer HW, Kievsky A. *Few-Body Syst.* 60:40 (2019)
72. Álvarez-Rodríguez R, Deltuva A, Gattobigio M, Kievsky A. *Phys. Rev. A* 93:062701 (2016)

73. Kharchenko VF. *Sov. J. Nucl. Phys.* 16:173 (1972)
74. Kievsky A, Gattobigio M. *Phys. Rev. A* 87:052719 (2013)
75. Kievsky A, Timofeyuk NK, Gattobigio M. *Phys. Rev. A* 90:032504 (2014)
76. Gattobigio M, Kievsky A. *Phys. Rev. A* 90:012502 (2014)
77. Kievsky A, Gattobigio M. *Phys. Rev. A* 92:062715 (2015)
78. Gogolin AO. *Phys. Rev. Lett.* 100:140404 (2008)
79. Deltuva A, Gattobigio M, Kievsky A, Viviani M. *Phys. Rev. C* 102:064001 (2020)
80. Hiyama E, Kamimura M. *Phys. Rev. A* 90:052514 (2014)
81. Kievsky A, et al. *Phys. Rev. A* 102:063320 (2020)
82. Efimov V. *Sov. J. Nucl. Phys.* 29:546 (1979)
83. Carbonell J, Deltuva A, Lazauskas R. *Comp. Rend. Phys.* 12:47 (2011)
84. Deltuva A. *Phys. Rev. C* 102:034003 (2020)
85. Kievsky A, Gattobigio M. *Few-Body Syst.* 57:217 (2016)
86. Gattobigio M, Kievsky A, Viviani M. *Phys. Rev. C* 100:034004 (2019)
87. Phillips AC. *Rep. Prog. Phys.* 40:905 (1977)
88. Rakityansky SA, Sofianos SA, Elander N. *J. Phys. A* 40:14857 (2007)
89. Girard BA, Fuda MG. *Phys. Rev. C* 19:579 (1979)
90. Orlov YV, Nikitina LI. *Phys. At. Nucl.* 69:607 (2006)
91. Adhikari SK, Fonseca AC, Tomio L. *Phys. Rev. C* 27:1826 (1983)
92. Rupak G, Vaghani A, Higa R, van Kolck U. *Phys. Lett. B* 791:414 (2019)
93. Lewerenz M. *J. Chem. Phys.* 106:4596 (1997)
94. Deltuva A. *Phys. Rev. A* 82:040701(R) (2010)
95. Gattobigio M, Kievsky A, Viviani M. *Phys. Rev. A* 84:052503 (2011)
96. Gattobigio M, Kievsky A, Viviani M. *Phys. Rev. A* 86:042513 (2012)
97. Deltuva A. *Phys. Rev. A* 85:042705 (2012)
98. Deltuva A. *Few-Body Syst.* 54:569 (2013)
99. Greene CH. *Phys. Today* 63:40 (2010)
100. Kievsky A, Gattobigio M, Timofeyuk NK. *Few-Body Syst.* 55:945 (2014)
101. Bazak B, Eliyahu M, van Kolck U. *Phys. Rev. A* 94:052502 (2016)
102. D'Incao J, von Stecher J, Greene C. *Phys. Rev. Lett.* 103:033004 (2009)
103. von Stecher J, D'Incao JP, Greene CH. *Nat. Phys.* 5:417 (2009)
104. von Stecher J. *J. Phys. B* 43:101002 (2010)
105. Pandharipande VR, et al. *Phys. Rev. Lett.* 50:1676 (1983)
106. Aziz RA, et al. *J. Chem. Phys.* 70:4330 (1979)
107. Kievsky A, Polls A, Juliá-Díaz B, Timofeyuk NK. *Phys. Rev. A* 96:040501(R) (2017)
108. van Kolck U. *Few-Body Syst.* 58:112 (2017)
109. Tan S. *Ann. Phys.* 323:2952 (2008)
110. Tan S. *Ann. Phys.* 323:2971 (2008)
111. Weiss R, Bazak B, Barnea N. *Phys. Rev. Lett.* 114:012501 (2015)
112. Weiss R, Pazy E, Barnea N. *Few-Body Syst.* 58:9 (2017)
113. Garrido E, Gattobigio M, Kievsky A. *Phys. Rev. A* 88:032701 (2013)
114. Ji C, Braaten E, Phillips DR, Platter L. *Phys. Rev. A* 92:030702(R) (2015)
115. Platter L, Hammer HW, Meißner UG. *Phys. Lett. B* 607:254 (2005)
116. Gattobigio M, Kievsky A, Viviani M. *Phys. Rev. C* 83:024001 (2011)
117. Hammer HW. *Few-Body Syst.* 59:58 (2018)
118. Pudliner BS, Pandharipande VR, Carlson J, Wiringa RB. *Phys. Rev. Lett.* 74:4396 (1995)
119. Kievsky A, Viviani M, Gattobigio M, Girlanda L. *Phys. Rev. C* 95:024001 (2017)
120. Lepage GP. How to renormalize the Schrödinger equation. In *Nuclear Physics: Proceedings of the VIII Jorge André Swieca Summer School, 1995*, ed. CA Bertulani, et al., pp. 135–80. Singapore: World Sci. (1997)
121. Lepage GP. The analysis of algorithms for lattice field theory. In *From Actions to Answers: Proceedings of the 1989 Theoretical Advanced Study Institute in Elementary Particle Physics*, ed. TA DeGrand, D Toussaint, pp. 97–120. Singapore: World Sci. (1989)

122. Entem DR, Machleidt R. *Phys. Rev. C* 68:041001 (2003)
123. Entem DR, Machleidt R, Nosyk Y. *Phys. Rev. C* 96:024004 (2017)
124. Epelbaum E, Krebs H, Meißner UG. *Phys. Rev. Lett.* 115:122301 (2015)
125. Epelbaum E, Meißner UG, Glöckle W. *Nucl. Phys. A* 714:535 (2003)
126. Gattobigio M, Kievsky A, Viviani M. *Few-Body Syst.* 54:657 (2013)
127. Kievsky A, et al. *Phys. Rev. Lett.* 121:072701 (2018)
128. Bombaci I, Logoteta D. *Astron. Astrophys.* 609:A128 (2018)
129. Logoteta D, Bombaci I, Kievsky A. *Phys. Rev. C* 94:064001 (2016)
130. Logoteta D, Bombaci I, Kievsky A. *Phys. Lett. B* 758:449 (2016)
131. Babenko VA, Petrov NM. *Phys. At. Nucl.* 63:1709 (2000)
132. Newton RG. *Scattering Theory of Waves and Particles*. Berlin/Heidelberg, Ger.: Springer (1982)
133. Girlanda L, Kievsky A, Viviani M, Marcucci LE. *Phys. Rev. C* 99:054003 (2019)
134. Girlanda L, Kievsky A, Marcucci LE, Viviani M. *Phys. Rev. C* 102:034007 (2020)

Annual Review of Nuclear and Particle Science

Volume 71, 2021

Contents

Errata

An online log of corrections to *Annual Review of Nuclear and Particle Science* articles may be found at http://www.annualreviews.org/errata/nucl